Eur. Phys. J. B **17**, 391–403 (2000)

THE EUROPEAN PHYSICAL JOURNAL B

EDP Sciences

Reordering kinetics of ion-disordered Ni_3Al

J.C. Ewert and G. Schmitz[a]

Institut für Materialphysik und SFB 345 der Universität Göttingen, Hospitalstrasse 3-7, 37073 Göttingen, Germany

Received 6 December 1999 and Received in final form 23 June 2000

Abstract. A study of the reordering kinetics of ion-irradiated Ni_3Al is presented. The development of long-range order during annealing treatments is measured by quantitative electron diffractometry. According to the temperature dependence of the observed kinetics, the reaction is dominated by non-equilibrium vacancies. As a consequence, the kinetics can be calibrated *versus* the absolute number of atomic jumps necessary to establish the observed degree of order. In order to analyse the experimental data, Monte Carlo simulations are performed. It is shown that, beside the temperature dependence of the driving force, the ordering efficiency of the vacancy jumps itself is temperature dependent due to different mobilities of the atomic species.

PACS. 81.30.Hd Constant-composition solid-solid phase transformations: polymorphic, massive, and order disorder – 64.60.Cn Order-disorder transformations; statistical mechanics of model systems – 02.70.Lq Monte Carlo and statistical methods – 61.80.Jh Ion radiation effects

1 Introduction

Due to their common microscopic mechanism, ordering and diffusion are strongly related phenomena. Thus, together with the growing understanding of atomic transport in intermetallic compounds, the microscopic mechanism of ordering also attracts considerable attention. For experimental studies on ordering, systems with an ordering temperature much below the melting point (*e.g.* Cu_3Au) are preferred because in this case the order may be widely varied when the critical temperature is approached. The situation is quite different in the case of Ni_3Al which is studied in this work. As the hypothetical ordering temperature is determined to be $T_c = 1723$ K [1], above the melting point of $T_m = 1668$ K, only minor variations of the order degree are obtained by thermal treatments. On the other hand, the high critical temperature allows study of the order reactions even at temperatures below $0.5\,T_c$, where the ordering tendency is very strong and in consequence the sublattice structure is very well defined. A potential influence of different activation barriers for vacancy jumps on the distinct sublattices should be emphazised under this condition.

A rather clear picture was already developed concerning the long-range atomic transport in Ni_3Al. Ni as well as Al atoms move on the coherent Ni sublattices by an ordinary vacancy mechanism. Structural vacancies, jump cycles or triple defects do not play an essential role [2]. By contrast, the microscopic ordering mechanism is still not understood. In near equilibrium studies, where only very small variations of order are traced by sensitive resistometry, two relaxation processes with different time constants are observed although nucleation and growth processes can be ruled out [3,4]. It has been suggested that these two processes are related to different antisite-vacancy pairs. However, this explanation is still not convincing as no statistical analysis on the number of the resulting jump sequences was given.

To investigate order relaxations starting far from equilibrium, Ni_3Al specimens may be disordered by athermal processes as melt-spinning [5], condensation to cooled substrates [6], ball milling [7–10], or electron irradiation [11–13]. With all these methods, the production of additional lattice defects is unavoidable. In this work, a disordered initial state is prepared by irradiation with 300 keV Ni ions. This way, lattice defects are produced in a rather controlled manner. Furthermore compared to electrons, complete disordering is possible at higher temperatures which keeps the concentration of interstitials very low, whereas a high density of non-equilibrium vacancies is preserved. Due to the vacancy supersaturation, the reordering kinetics can be studied at very low temperatures where the atomic mobility would be frozen under thermal conditions. The disordering process itself is studied in recent work [14–16].

The development of the long-range order (LRO) during an annealing treatment subsequent to the irradiation is evaluated by means of electron diffraction. In general, diffraction methods are advantageous as, in contrast to resistometry or calorimetry, the signal is not influenced by the concurrent annealing of microstructural defects.

[a] e-mail: guido@umpa02.gwdg.de

Due to the small penetration depth of the ions, the irradiated volume is very small so that X-ray diffraction is not feasable. Instead, the irradiated specimen zone is easily investigated by microdiffraction inside an electron microscope.

In order to interprete the experimental results, the time development of the point defect concentrations is evaluated and the observed kinetics is compared with the statistical predictions of Monte-Carlo (M.C.) simulations.

2 Experimental methods

2.1 Sample preparation

A Ni_3Al alloy was produced from pure aluminium (99.999%) and nickel (99.999%) by inductance melting under argon atmosphere. The material was homogenized and long-range ordered by annealing at 1100 °C for 7 days. The composition of the material was determined to 24 ± 1 at% Al by microprobe analysis. As the penetration depth of the ion beam is very limited, electron transparent foils were prepared prior to the irradiation treatment. For which disks of 3 mm diameter were spark eroded, mechanically ground to 150 μm and thinned by ordinary jet-polishing using an electrolyte of 50 ml perchloric and 950 ml acetic acid at 15 °C and 90 V cell voltage.

2.2 Ion irradiation

Specimens were irradiated with 300 keV ^{58}Ni ions at room temperature using the implanter IONAS [17] at the university of Göttingen. In order to calibrate the irradiation damage, simulations with the 'TRIM' software [18] were performed. The displacement cross-section and the depth of the damaged zone were calculated to be $\sigma_d = 1.65 \times 10^{-19}$ m^2 and about 100 nm, respectively. Thus, the electron tranparent foils are homogeneously damaged throughout their thickness of 50 nm. The foils were completely disordered by irradiation up to a dose of 1 dpa [16] at a displacement rate of 10^{-3} dpa/s corresponding to a beam current of 100 nA/cm^2. Homogeneous beam intensity was guaranteed over an area of 10×10 mm^2 by an electrostatic x-y beam sweeping system. The target was water cooled during the irradiation.

2.3 Transmission electron microscopy

Irradiated Ni_3Al specimens were examined with a *Philips EM420ST* microscope at an acceleration voltage of 120 kV. The reordering experiments were performed inside the microscope using a *GATAN* double tilt heating stage. The specimen temperature was determined by a thermocouple directly clamped to the specimen furnace. As the heat conductivity in the electropolished metallic specimens is rather good, the accuracy of the temperature measurement is supposed to be ± 10 K. Starting at room temperature, the annealing temperature of the isothermal treatment is reached according to an exponential time law, with a time constant of 60 s. Ni_3Al is a preferred high temperature structural material because of its high corrosion resistance. This property turns out to be advantageous for the *in situ* heat treatments as the specimens stay very stable and show only minor effects of erosion during the annealing. By choosing sufficiently high annealing temperatures almost complete recovery of LRO is achieved (see Fig. 7b).

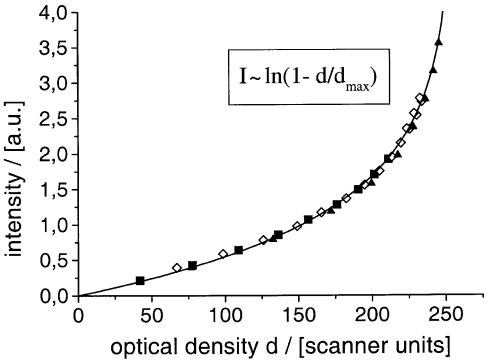

Fig. 1. Densitometric transfer function of negative material and CCD scanner. By several independent series of exposures, represented by different symbols, the reproducibility of film development and the digitizing procedure is confirmed.

The formation of the ordered zones was studied during the heat treatment by dark field imaging based on {110}-superlattice reflections. The evolution of the long-range order parameter was determined by electron diffractometry. For that, low indexed zone axis orientations were always chosen to achieve reproducible quantitative results. Diffraction patterns were recorded on conventional micrographs which were evaluated with a CCD scanner taking the characteristics of the film material into account. The experimentally determined transfer function is shown in Figure 1. It is in excellent agreement with the logarithmic relation

$$I = I_0 \ln(1 - g), \tag{1}$$

where I, I_0, and g denote the electron intensity, a suitable normalization constant, and the grey value relative to that of complete saturation, respectively. As we are only interested in intensity ratios, the actual value of I_0 is of no importance. In order to obtain a sufficient sensitivity of measurement, short exposure times are chosen, so that the relative grey levels of interesting intensities never exceed 80% and the approximately linear regime of the transfer function is utilized.

When electron diffraction intensities have to be quantitatively interpreted, dynamical beam interactions must be taken into account. Thus, the standard methods established for X-ray diffraction must not be used. The evaluation scheme which was applied in this study is presented in more detail in the next section.

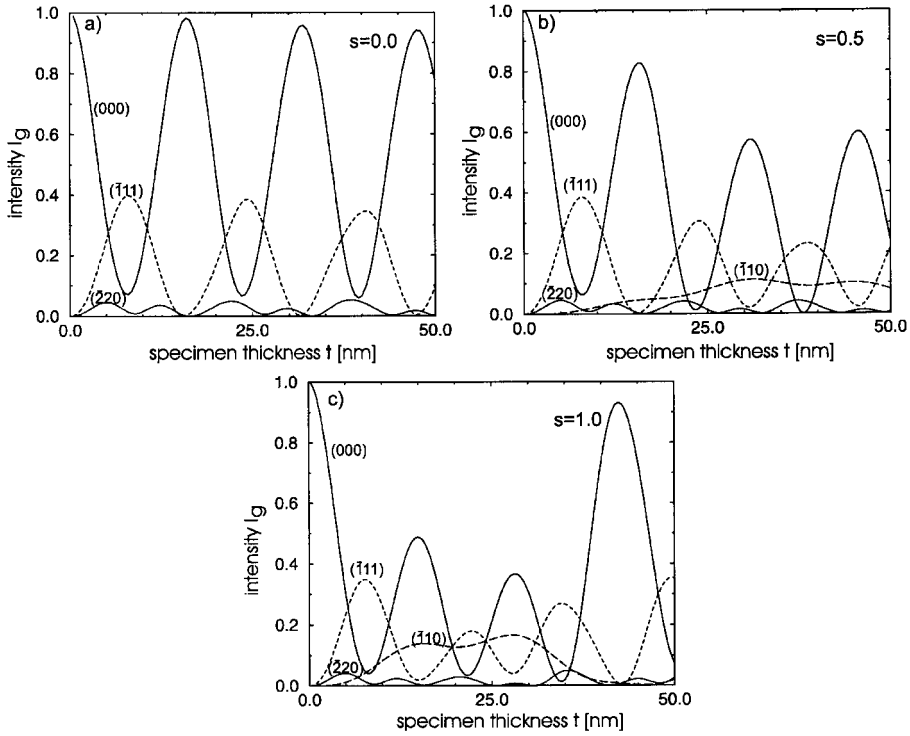

Fig. 2. Intensities of various reflections *versus* specimen thickness. Calculation for Ni_3Al in [112] zone axis orientation, using an electron image simulation program [23]. The figures display the intensities for three different order parameters, $s = 0$, $s = 0.5$, and $s = 1.0$, respectively.

3 Electron diffractometry

Although a correct evaluation of its intensity is complicated, electron diffraction had been used in the past to measure long-range order of intermetallic compounds, especially in the case of electron irradiation experiments, *e.g.* [11,12,19,20]. Most of these studies were based on the intensity ratio between a superlattice and a fundamental reflection using the kinematic relation

$$\frac{I_{\mathrm{S}}}{I_{\mathrm{F}}} \propto s^2, \tag{2}$$

where s is the LRO parameter. However, Urban [21] pointed out by numerical calculations that this expression is invalid under dynamical diffraction conditions and may be only used for very thin specimens and light elements. The shortcoming of the kinematic description becomes particular clear when the numerical values of the intensity ratio are considered. For completely ordered Ni_3Al in kinematic approximation, the intensity ratio I_{110}/I_{220} is given by the corresponding structure factors $G_{(110)} = f_{\mathrm{Al}} - f_{\mathrm{Ni}}$ and $G_{(220)} = (f_{\mathrm{Al}} + 3f_{\mathrm{Ni}})$. Taking the appropriate atomic scattering factors f_{i} from tabulated data [22], we expect

$$(I_{110}/I_{220})_{(s=1)} = G^2_{(110)}/G^2_{(220)} = 0.036. \tag{3}$$

Thus, the superlattice reflection should amount to only a few percent of the fundamental reflection. By contrast, we actually observe the superlattice reflection even stronger than the fundamental one in the experiment. Averaging the experimental intensities over a suitable specimen thickness range, as will be explained below,

$$(I_{110}/I_{220})_{(s=1)} = 3.1 \pm 0.2 \tag{4}$$

is found for well annealed Ni_3Al investigated in [112] zone axis orientation.

In Figure 2 diffracted intensities are plotted *versus* foil thickness for three different LRO parameters, calculated with the simulation software EMS [23]. Beside the amplitude of the intensity oscillations, also the oscillation periods vary with the order parameter which demonstrates that equation (2) is obviously in error. In order to deduce the LRO parameter from a ratio of reflection intensities, in principle the foil thickness must be known to a nm accuracy, which cannot be achieved experimentally. However, a reliable analysis may be obtained when the diffracted intensities are averaged over a suitable thickness range.

The thickness averaged intensity may be calculated in the conventional Bloch wave formalism, see *e.g.* [24]. Inside the crystal the electron wave is split into Bloch waves of different wavelength causing the thickness oscillations of the intensity. In the case of a low indexed zone axis orientation, the electron wave $\Psi(r)$ propagating parallel to the axis is described by

$$\Psi(r) = \sum_j \epsilon^{(j)} B^{(j)}(r); \quad B^{(j)}(x,z) = \mathrm{e}^{\mathrm{i}k_j z} \sum_g C_g^{(j)} \mathrm{e}^{\mathrm{i}gx}, \tag{5}$$

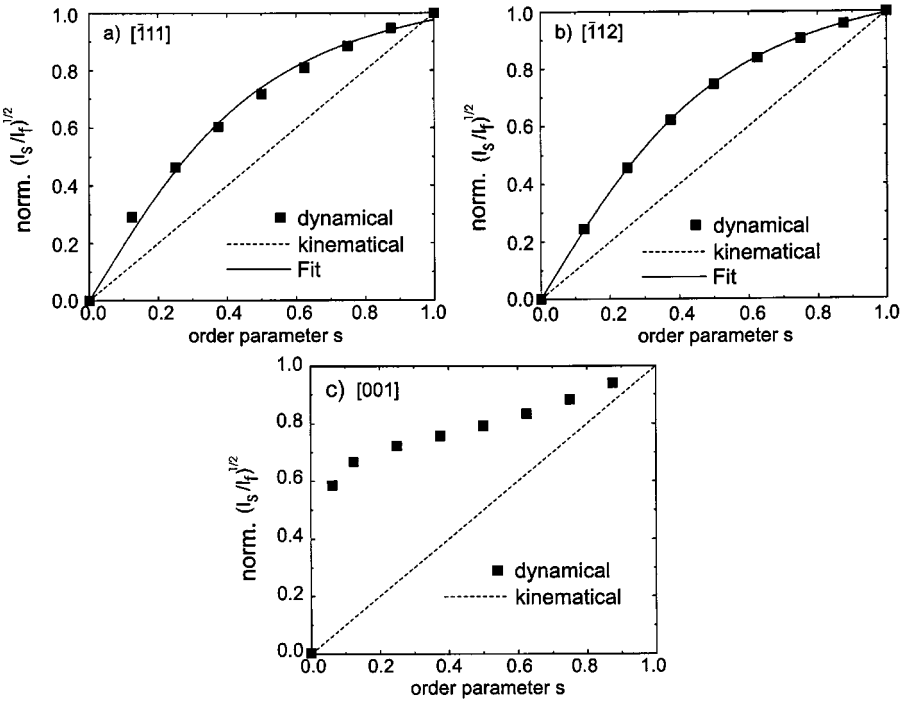

Fig. 3. Ratio between the thickness integrated intensity of the (110) and (220) reflections *versus* long-range order. Ni-25 at%-Al in [$\bar{1}$11], [$\bar{1}$12], and [001] zone axis orientation, respectively. It is obvious that the slope of the curve depends strongly on the chosen orientation. Squares indicate results of the dynamical calculation. The dashed line represents the kinematic relation (Eq. (2)), the solid line the model according to equation (9).

where $B^{(j)}$ represents a certain Bloch wave given by a linear combination of plane waves with lateral reciprocal lattice vectors g and expansion coefficients $C_g^{(j)}$, and x and z are the lateral and normal component of the position. The excitation $\epsilon^{(j)}$ of a Bloch state is easily shown to be equivalent to its zero beam component $C_0^{(j)}$. Thus neglecting absorption, the intensity of a reflection g in the diffraction pattern is given by

$$I_g(z) = \sum_j \sum_l C_0^{(j)} {C_0^{(l)}}^* C_g^{(j)} {C_g^{(l)}}^* \mathrm{e}^{\mathrm{i}(k_j - k_l)z} \,. \qquad (6)$$

In the case of symmetrical zone axis orientations, only a few Bloch waves with different wave vectors are excited [25]. Consequently, the phase factors $\exp[\mathrm{i}(k_j - k_l)z]$ of mixed terms ($j \neq l$) in equation (6) cancel out by the thickness integration and the averaged intensity is obtained by:

$$\frac{1}{\Delta z} \int_{z_\mathrm{i}}^{z_\mathrm{f}} I_g(z) \mathrm{d}z = \sum_j |C_0^{(j)}|^2 |C_g^{(j)}|^2 \,, \qquad (7)$$

where the structure dependent expansion coefficients are most easily calculated using the simulation software (*e.g.* EMS). Considering again completely ordered Ni_3Al in {112} zone axis orientation, the dynamical calculation predicts an intensity ratio

$$(I_{110}/I_{220})_{(s=1)} = 4.9 \,. \qquad (8)$$

Thus, the intensity of the superlattice reflection is indeed expected to exceed that of the fundamental reflection. Comparing the numerical values in equations (3, 4, 8), the significant improvement by the dynamical calculation becomes obvious. However, still a considerable deviation between experimental data and theoretical prediction must be stated, which may be explained by the neglection of absorption effects, deficits in the atomic scattering factors, and of course also by a deviation of the specimen composition from stoichiometry. In consequence, in order to determine the degree of LRO, one has to rely on relative measurements comparing the intensity ratio of the specimen state under consideration to that of well annealed specimens, as is often similarly done in X-ray diffractometry.

In Figure 3 dynamically calculated intensity ratios I_{011}/I_{022}, normalized to the state of complete order, are plotted *versus* the LRO parameter for three different zone axis specimen orientations. The kinematic relation (Eq. (2)) is shown by the dashed line for comparison. The large difference between the kinematic and the dynamic result is obvious. Furthermore, the dynamic relation depends on the orientation, which may be utilized by the experiment. The [001] orientation shows an excellent sensitivity for the determination of small order parameters, but will be insensitive for larger ones. By contrast, the [112] and [111] orientations exhibit useful sensitivities over the whole range of order. The intensity ratios of the latter orientations are reasonably fitted by the analytical

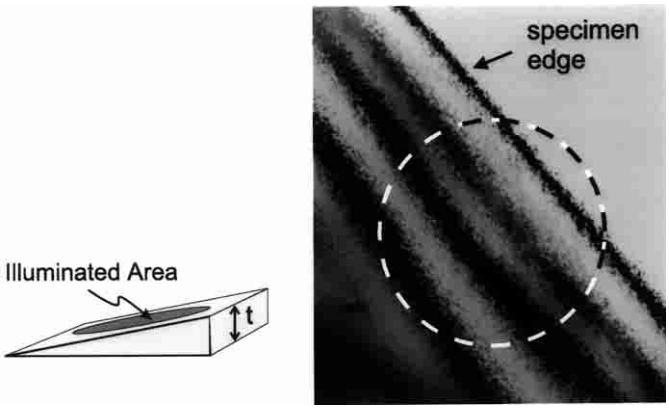

Fig. 4. Thickness average of scattered intensities at a wedge-shaped specimen. The size of the selected area aperture is chosen so that a region of at least three subsequent extinction contours contribute to the diffraction pattern as shown on the right.

expression

$$\frac{(I_{110}/I_{220})_s}{(I_{110}/I_{220})_{(s=1)}} = (1+a^2)\frac{s^2}{1+a^2s^2}\,, \qquad (9)$$

as is demonstrated by the solid lines in Figures 3a, b. The numerical parameter a describes the deviation from the kinematic approximation. A [112] zone axis orientation was always chosen for the measurements presented in this work. We use equation (9) instead of equation (2) to determine the LRO parameter from the intensity data. The necessary model parameter is adapted to the dynamical calculation shown in Figure 3b to be $a = 1.72$. It should be noted that to our present understanding the analytical relation represented by equation (9) does not have any deeper physical justification. It represents just a mathematical tool to facilitate the data interpretation under the particular experimental condition. Consequently, the model parameter a is valid only for the material and the specimen orientation investigated here. To apply the presented method to other situations, the calculation of the intensities according to equation (7) always forms the appropriate basis.

In the experiment, the thickness averaging of the scattered intensities is realized at specimen wedges as illustrated in Figure 4. Using the selected area diffraction (SAD) aperture, a suitable specimen region is chosen for analysis, so that diffracted intensities of a continuous thickness range are collected. Due to the varying specimen shape and the limited number of accessible aperture sizes, the actual thickness range of averaging varies from measurement to measurement. However, to our experience, reproducible intensity ratios with an accuracy better than 5% result if the SAD aperture contains at least a region of four extinction contours. In other words, the exact specimen thickness must not be known to obtain reliable data, as long as each measurement records a thickness range larger than about 40 nm. In order to determine the appropriate aperture size, extinction contours were imaged in the exact zone axis direction. The typical size and position of the SAD aperture is indicated in Figure 4. Thin specimen areas are preferred for the analysis in order to reduce the diffuse background of the diffraction patterns.

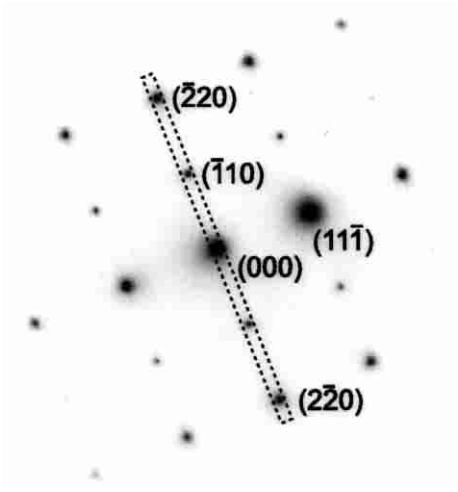

(a)

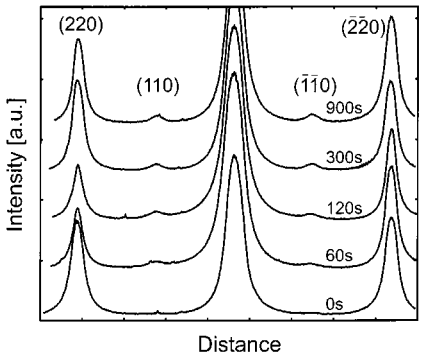

(b)

Fig. 5. (a) Diffraction pattern of Ni_3Al in [112] zone axis orientation. (b) diffraction spectra during a reordering treatment at $T = 573$ K. The superlattice reflections grow with increasing time.

An example of a diffraction pattern in [112] orientation is shown in Figure 5a. The intensity is evaluated inside the marked stripe to obtain spectra as presented in Figure 5b. In order to determine the reflection intensity, the diffuse background was subtracted and the intensities of symmetric reflections, *e.g.* $(\bar{2}20)$ and $(2\bar{2}0)$ were added to reduce the effect of eventual misalignments. As discussed above, the intensity of the superlattice reflections is comparable to that of the fundamental ones under dynamical scattering conditions. Thus, although the dynamic range of the film material is limited, the necessary intensity ratios are still determined with sufficient accuracy. Provided that the ordered domains do not become too small, the method is able to detect order parameters down to $s = 0.02$.

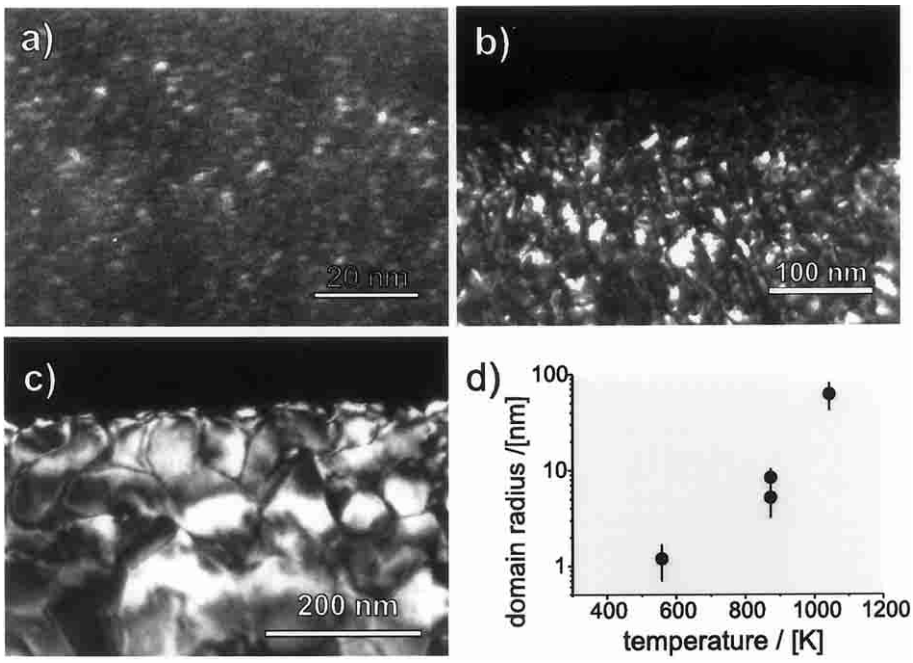

Fig. 6. Dark field electron microscopy of annealed specimens: (a) 473 K/3600 s, $s = 0.08$; (b) 698 K/4000 s, $s = 0.22$; (c) 1043 K/8000 s, $s = 0.91$. The average domain radius is plotted *versus* the temperature in (d).

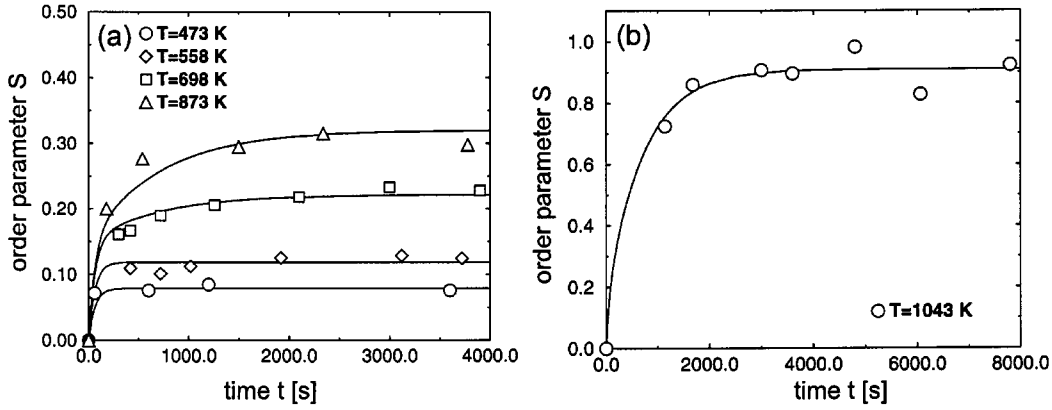

Fig. 7. Development of the long-range order parameter s of Ni_3Al during an isothermal annealing. (a) Annealing temperatures $T = 473$ K, $T = 558$ K, $T = 698$ K, and $T = 873$ K. (b) $T = 1043$ K.

4 Results

The ion-disordered specimens do not show any tendency for natural reordering even after several months of room temperature storage. The onset of the reordering reaction is observed above 373 K. Specimens were isothermally annealed at various temperatures between 473 and 1043 K for up to 8000 s. During this heat treatment, the specimens order by a domain growth mechanism as is demonstrated by the (011) dark field micrographs presented in Figure 6. At the beginning of heat treatment, the ordering reaction takes place very fast but then an apparent metastable state is established which does not develop further without increasing the temperature. Consequently, the domain size is mainly controlled by the annealing temperature as shown in Figure 6d. The development of the LRO parameter, determined from the diffraction patterns as explained above, is shown in Figure 7. Even at the lowest investigation temperature (473 K), the initial part of the reaction proceeds with a time constant comparable to the heating constant of the specimen furnace. Thus, the detailed kinetics of this reaction stage cannot be resolved. During the available measuring time, a temperature dependent plateau value of the degree of order is reached which still significantly deviates from the corresponding equilibrium LRO parameter. In order to establish a degree of order comparable to that of thermal equilibrium, annealing temperatures above 1 000 K are necessary.

Table 1. Parameters of pure Ni necessary for the calculation of point defect densities and mobilities [2,28,36]. (ΔS^{f} denotes the vacancy formation entropy and D_0 the prefactor of the Ni tracer diffusion coefficient.)

$E_{\mathrm{v}}^{\mathrm{f}}$	ΔS^{f}	$E_{\mathrm{v}}^{\mathrm{m}}$	D_0	$E_{\mathrm{i}}^{\mathrm{M}}$	$D_{\mathrm{v}}(RT)$	$D_{\mathrm{i}}(RT)$	$\dot{\Phi}$	k_0	L
eV	k_B	eV	cm^2/s	eV	m^2/s	m^2/s	dpa/s	1/s	nm
1.8	≈ 1.5	1.11	1.3	0.15	10^{-25}	10^{-8}	10^{-3}	1.5×10^{-5}	20

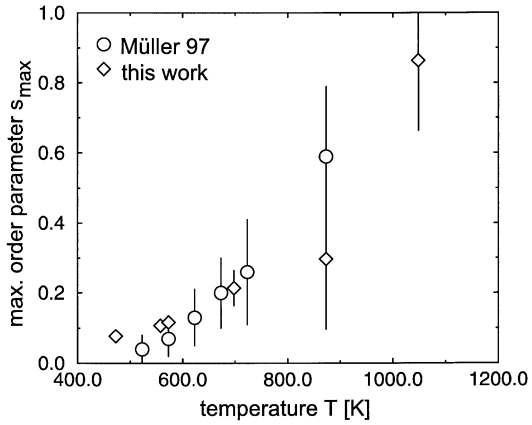

Fig. 8. Order parameter $s_{\max}$, after 3600 s annealing at different temperatures. For comparison, data of Müller [26] is also shown, obtained from specimens which were irradiated to 10 dpa at 200 K.

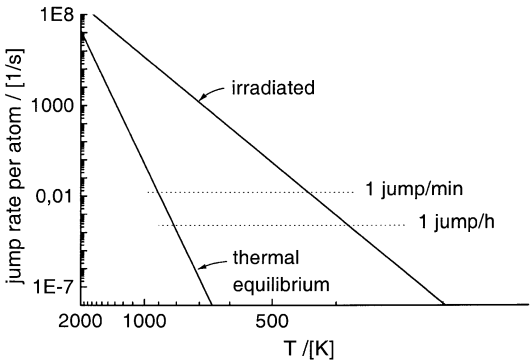

Fig. 9. Atomic jump frequency *versus* temperature. The frequency in thermal equilibrium is calculated from the diffusion data of pure Ni (Tab. 1). In the case of irradiated specimens, a vacancy concentration of 10^{-3} is assumed.

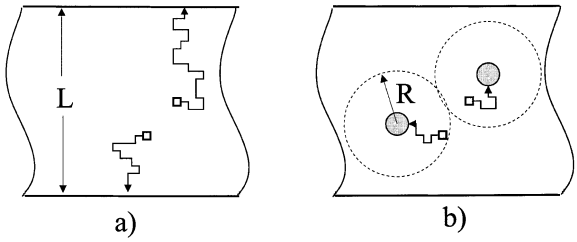

Fig. 10. Annealing mechanisms for ion-induced vacancies. (a) Surface sinks, the total number of atomic jumps during annealing is determined by the specimen thickness. (b) Vacancy clusters, the number of atomic jumps decreases dependent on the cluster density.

The plateau values of the LRO parameter are plotted *versus* the annealing temperature in Figure 8. For comparison, results of a recent independent measurement of ion-disordered Ni_3Al [26] are also shown. Although the disordering conditions of those experiments and the evaluation of the diffraction intensity were somewhat different, the results are quite comparable confirming the reliability of our method. The *in situ* measurements of this work using a heating stage inside the microscope have the important advantage that the temporal evolution of the order may be determined easily. In this way, the interesting characteristics of the order kinetics, *i.e.* fast initial reaction, non-equilibrium plateau value, become obvious.

5 Reordering kinetics

At first sight the evolution of the LRO is quite remarkable due to the very low reaction temperatures and the establishment of an apparent steady state, characterized by order degrees much below one. This behaviour can hardly be explained by a reaction mechanism based on thermal vacancies. In Figure 9 the number of thermal jumps per atom is plotted *versus* the temperature, calculated from diffusion data in the literature of pure Ni (see Tab. 1). Reasonable mobilities, *e.g.* one jump per atom, which could explain a measurable ordering effect within the observation time, are only reached above 900 K.

On the other hand, if the ordering reaction were dominated by the motion of ion-induced non-equilibrium point defects, at first the observed temperature dependence of the plateau values is astonishing. The initial density of point defects is identical in all annealing experiments. Thus, being only a function of the geometry, the total number of vacancy or interstitial jumps towards the surface sinks should be independent of the temperature as sketched in Figure 10a. In addition, the thermodynamic driving force for ordering decreases with increasing temperature so that, if there were any temperature dependence at all, the degree of order would only become smaller with increasing temperature.

In order to still explain the observed temperature dependence of the order plateaus, two different mechanisms may be postulated: (i) the number of atomic jumps is reduced at low temperatures by the nucleation of sessile point defect clusters in sufficient density (see Fig. 10b), or (ii) the ordering efficiency of an atomic jump itself increases with temperature. In order to explain the experimental observation quantitatively by mechanism (i), very

small vacancy clusters would have to be assumed to be stable and sessile, which is not reasonable as the binding energy of a vacancy pair amounts to only 0.1 eV [27], and additionally in fcc materials the migration enthalpy of pairs is even smaller than that of single vacancies [28]. Thus mechanism (ii) is considered to be responsible for the oberserved temperature dependence. In the following, quantitative arguments are presented to support this interpretation.

5.1 Density of non-equilibrium point defects

In order to understand the reordering kinetics, the atomic density of mobile, non-equilibrium point defects introduced by the irradiation must be known. A thorough estimate may be obtained by well established rate equations [29] for the number of vacancies and interstitials

$$\frac{\mathrm{d}c_\mathrm{v}}{\mathrm{d}t} = k_0 - k_\mathrm{r}(D_\mathrm{i} + D_\mathrm{v})c_\mathrm{i}c_\mathrm{v} - k_\mathrm{s}D_\mathrm{v}c_\mathrm{v} \qquad (10)$$
$$\frac{\mathrm{d}c_\mathrm{i}}{\mathrm{d}t} = k_0 - k_\mathrm{r}(D_\mathrm{i} + D_\mathrm{v})c_\mathrm{i}c_\mathrm{v} - k_\mathrm{s}D_\mathrm{i}c_\mathrm{i},$$

where k_0 denotes the generation rate of mobile vacancies or interstitials, $k_\mathrm{r} \approx 8\pi a_0/\Omega$, k_s the strength of fixed sinks and D_v, D_i, a_0, and Ω the diffusion constant of vacancies and interstials, lattice constant, and the atomic volume, respectively. In the case of irradiation with 300 keV Ni ions, only 1.5% of the displacements result in the formation of mobile Frenkel defects [30]. Regarding the thin specimen foils, the most effective sinks are the surfaces. Thus, the sink strength is given by $k_\mathrm{s} = \pi^2/L^2$ [31], where L is the thickness of the specimen. For the diffusivities of the point defects, parameters of pure Ni are used. This practice is justified as the vacancy formation as well as the migration enthalpy of Ni is very similar to that of ordered Ni_3Al and data of non-equilibrium disordered Ni_3Al alloys is not known, anyway. Quantitative parameters following from these considerations are shown in Table 1.

Due to the low vacancy mobility and the high sink density, the steady state of equations (10) is not reached during the irradiation. Instead a quasi-steady state is established, characterized by a competition between the annihilation of interstitials at the surface sinks and the recombination of interstitials with vacancies. In this regime the point defect densities are estimated by [29]

$$c_\mathrm{v}^0 \approx \sqrt{\frac{\pi k_0 a_0^2}{32L^2}t}\,; \quad c_\mathrm{i}^0 \approx \sqrt{\frac{k_0}{k_\mathrm{r}k_\mathrm{s}D_\mathrm{i}^2}\frac{1}{t}}\,. \qquad (11)$$

Thus, after irradiation up to a fluence of 1 dpa, the vacancy and interstitial densities amount to $c_\mathrm{v} = 0.7 \times 10^{-3}$ and $c_\mathrm{i} = 3 \times 10^{-15}$, respectively. It should be noted that the vacancy concentration as given by equations (11) is essentially determined by well known geometrical parameters. Room temperature mobilities, which can be hardly measured experimentally, do not influence it. Furthermore, the maximum density of vacancies is limited to $c_\mathrm{v}^\mathrm{max} = 0.01$ by the spontaneous recombination volume

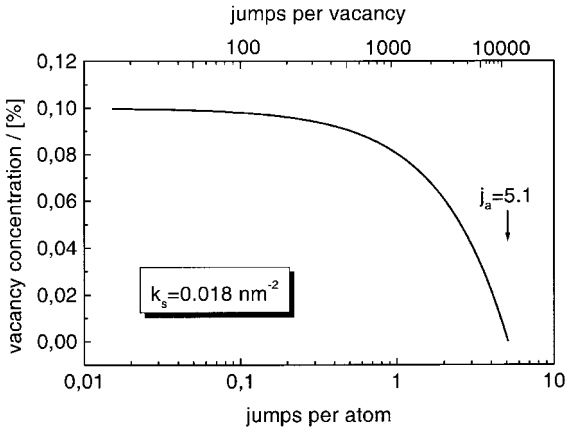

Fig. 11. Vacancy density during the annealing treatment calculated by equation (10), $K_\mathrm{S} = 0.018$ nm^{-2}. The upper x-axis represents a natural time scale as the jump frequency of the vacancies is nearly constant.

of about 100Ω surrounding each point defect. Thus, taking an eventual error of the defect generation rate into account, the vacancy concentration is at least reliably bound between $c_\mathrm{v}^0 = 10^{-4}$ and 10^{-2}. In the high dose limit, the formation of defect clusters may be assumed, which is neglected by equations (11). However in this case, the quantitative estimate will stay valid at least as an upper limit for the density of mobile vacancies. The estimated density of 10^{-3} is indeed sufficient to explain the observed low reaction temperatures which is clarified by Figure 9. A reasonable mobility of one jump per atom within the first minute of aging is predicted between 400 and 500 K.

On the other hand, the estimated interstitial concentration is much too low to induce significant reordering during the annealing, especially as interstitial jumps are supposed to have much smaller efficiency for reordering compared to vacancy jumps [32].

During the annealing treatment, non-equilibrium vacancies annihilate at the foil surfaces. Thus, the mobility per atom continuously decreases. The time dependent density is calculated with equation (10) using $k_0 = 0$ and $c_\mathrm{i} = 0$ as plotted in Figure 11. According to the diffusivity data of Table 1, the jump frequency of the vacancy at 473 K amounts to already 400/s. Thus, the annealing of the mobile vacancies shown in the figure takes only a few tens of seconds, which explains the observed very short reaction times required to reach the LRO plateau.

In order to understand the LRO plateaus, the maximum number of atom replacements allowing the system to reorder is important. This number is obtained by

$$\mathrm{d}j_\mathrm{a} = c_\mathrm{v}\nu_\mathrm{v}\mathrm{d}t = -\frac{\nu_\mathrm{v}}{k_\mathrm{s}D_\mathrm{v}}\mathrm{d}c_\mathrm{v} \qquad (12)$$
$$j_\mathrm{a}^\mathrm{max} = \int_{c_\mathrm{v}^0}^{0} c_\mathrm{v}\nu_\mathrm{v}\mathrm{d}t = \frac{12}{k_\mathrm{s}a_0^2}c_\mathrm{v}^0\,, \qquad (13)$$

where j_a and ν_v denote the number of jumps per atom and the jump frequency of the vacancies, respectively. Averaging the sink strength on the specimen wedge,

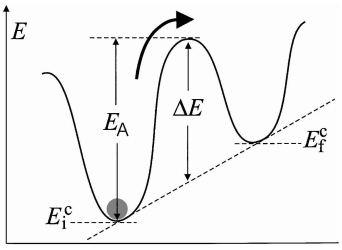

Fig. 12. Activation barrier defining the jump probabilities of the M.C. model.

$k_s = 3\pi^2/L_{max}^2 = 0.018\ nm^{-2}$, at most 5.1 replacements per atom are performed during the annealing.

5.2 Ordering efficiency of vacancy jumps

The ordering kinetics may be described by the phenomenological equation

$$ds = \alpha(s,T)\frac{\partial f}{\partial s} dj_a\,, \tag{14}$$

where $\partial f/\partial s$ is the thermodynamical driving force of the reaction and α describes the efficiency of the atomic jumps for ordering. Especially in the case of a first order transition, as present for the $L1_2$ superstructure, the ordering process starting from a completely disordered microstructure is quite complicated so that the functional dependence of α on the order degree or the temperature is difficult to predict. In general, the kinetics are expected to be a superposition of homogeneous ordering, in first approximation, modeled by a chemical rate theory as proposed by Dienes [33], a nucleation and growth mechanism as described by a Johnson-Mehl-Avrami (JMA) kinetics, and finally domain ripening. *A priori*, the sequence of these different reaction mechanisms is not known in detail. Therefore, in order to estimate the ordering efficiency of the atomic jumps, especially the potential temperature dependence, Monte-Carlo simulations are performed. In this case, all the different reaction stages are naturally taken into account. However the microscopic model selecting between possible atomic jumps must be considered carefully to obtain a realistic description of the kinetics. A system of 64^3 lattice sites with periodic boundary conditions is used, occupied by one vacancy and the atoms of a stoichiometric alloy. In each Monte Carlo step, the vacancy exchanges its site with one of its twelve next neighbours, selected according to the probability of a particular jump. This probability is defined by

$$p_{i\to f} \propto \exp\left(-\frac{\Delta E + (E_f^c - E_i^c)/2}{kT}\right), \tag{15}$$

where E_i^c and E_f^c are the energy of the initial and final configuration, and ΔE determines the average height of the activation barrier (see also Fig. 12). This definition fulfills the principle of detailed balance. The choice of ΔE merely calibrates the time scale but does not influence the relative jump probabilities. As we are only interested in the order rate per average atomic jump, it may be conveniently set to zero.

Pair interactions up to at least the second nearest neighbour are necessary to stabilize the $L1_2$ superstructure. In order to calculate the remaining energy difference in equation (15), it is convenient to define a site energy as the energy obtained by placing an atom at a particular lattice site. For the case of a Ni atom next to the vacancy we have

$$\begin{aligned} E_{site}(\mathrm{Ni}) := {} & n_{site}^{(1)}\,\epsilon_{NiAl}^{(1)} + (z^{(1)} - n_{site}^{(1)} - 1)\,\epsilon_{NiNi}^{(1)} \\ & + n_{site}^{(2)}\,\epsilon_{NiAl}^{(2)} + (z^{(2)} - n_{site}^{(2)})\,\epsilon_{NiNi}^{(2)}\,, \end{aligned} \tag{16}$$

where $n_{site}^{(1)}$, $n_{site}^{(2)}$, $z^{(1)}$ and $z^{(2)}$ denote the number of Al atoms and the coordination number of the first and second neigbour shell around the particular site. Considering the Ni atom jumping from its initial site i into its final site f, the neighbouring vacant position, the related variation of configurational energy is calculated according to

$$(E_f^c - E_i^c)_{Ni} = E_f(\mathrm{Ni}) - E_i(\mathrm{Ni}) \tag{17}$$

$$\begin{aligned} &= (n_f^{(1)} - n_i^{(1)})(\epsilon_{NiAl}^{(1)} - \epsilon_{NiNi}^{(1)}) \\ &\quad + (n_f^{(2)} - n_i^{(2)})(\epsilon_{NiAl}^{(2)} - \epsilon_{NiNi}^{(2)}) \end{aligned} \tag{18}$$

$$\begin{aligned} &= (n_f^{(1)} - n_i^{(1)})(\epsilon^{(1)} - \epsilon_{AS}^{(1)}) \\ &\quad + (n_f^{(2)} - n_i^{(2)})(\epsilon^{(2)} - \epsilon_{AS}^{(2)})\,, \end{aligned} \tag{19}$$

where ϵ is the usual pair exchange parameter

$$\epsilon^{(i)} = \epsilon_{NiAl}^{(i)} - (\epsilon_{NiNi}^{(i)} + \epsilon_{AlAl}^{(i)})/2 \tag{20}$$

and ϵ_{AS} describes the asymmetry between pure Ni and Al bonds by

$$\epsilon_{AS}^{(i)} := (\epsilon_{NiNi}^{(i)} - \epsilon_{AlAl}^{(i)})/2\,. \tag{21}$$

The case of a jumping Al atom is treated in an analogous way resulting in

$$\begin{aligned} (E_f^c - E_i^c)_{Al} = {} & -(n_f^{(1)} - n_i^{(1)} - 1)(\epsilon^{(1)} + \epsilon_{AS}^{(1)}) \\ & -(n_f^{(2)} - n_i^{(2)} - 1)(\epsilon^{(2)} + \epsilon_{AS}^{(2)})\,. \end{aligned} \tag{22}$$

The representation in terms of pair exchange and asymmetry parameters is advantageous as only the former determine the equilibrium properties of the system. The asymmetry parameters do not influence the thermodynamics, but they essentially control the mobilities of the different species and thus the kinetics of the reaction.

Following a suggestion of Haider [34], the pair exchange potentials of first and second neighbour bonds are set to

$$\epsilon^{(1)} = -0.08\ \mathrm{eV}; \quad \epsilon^{(2)} = 0.032\ \mathrm{eV}, \tag{23}$$

which yields the correct thermodynamics of the ordering transition and represents the Ni-rich side of the Ni-Al phase diagram reasonably. In order to obtain a realistic

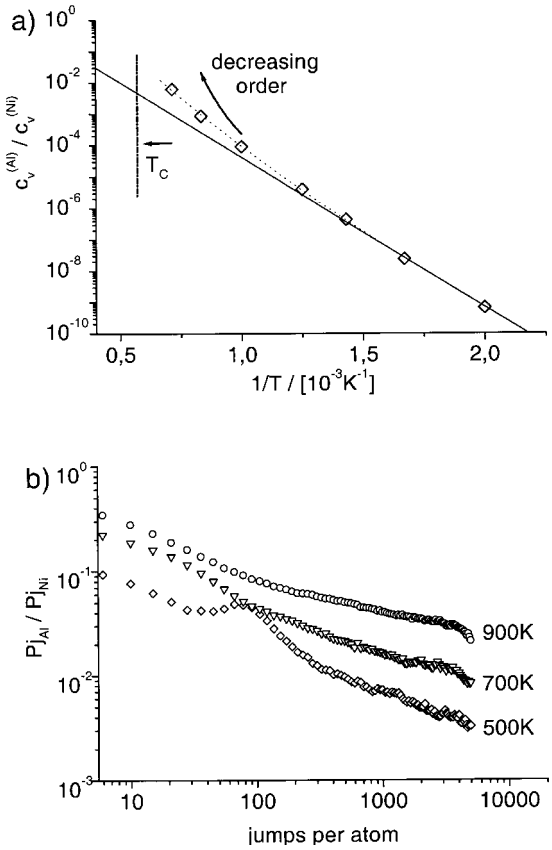

Fig. 13. Jump statistics of the M.C. model. (a) Ratio between the vacancy concentrations on the Al and the Ni sublattice *versus* temperature calculated for Ni_3Al in thermal equilibrium. (b) Ratio between the jump probabilities of the Al and Ni atoms during the reordering reaction.

model, the asymmetry parameters are adjusted to reproduce the difference of the vacancy formation enthalpies on the Ni sublattice and the Al sublattice, $E_{\mathrm{V}}^{(\mathrm{Al})} - E_{\mathrm{V}}^{(\mathrm{Ni})} = 0.8$ eV, as was determined recently by the local-density-functional method [27]. With

$$E_{\mathrm{V}}^{(\mathrm{Ni})} = \Delta E^{(\mathrm{Ni})} + \mu_{\mathrm{Ni}} \tag{24}$$

$$E_{\mathrm{V}}^{(\mathrm{Al})} = \Delta E^{(\mathrm{Al})} + \mu_{\mathrm{Al}} \tag{25}$$

and

$$\mu_{\mathrm{Al}} = E_0 + \frac{3}{8}(E_{\mathrm{Al}}^{(\mathrm{Ni})} - E_{\mathrm{Ni}}^{(\mathrm{Al})}) \tag{26}$$

$$\mu_{\mathrm{Ni}} = E_0 - \frac{1}{8}(E_{\mathrm{Al}}^{(\mathrm{Ni})} - E_{\mathrm{Ni}}^{(\mathrm{Al})}) \tag{27}$$

where ΔE, E_0, $E_{\mathrm{Al}}^{(\mathrm{Ni})}$, and $E_{\mathrm{Ni}}^{(\mathrm{Al})}$ represent the energy of the broken bonds related to the vacancy, the cohesion energy of the crystal, and the anti-site energies of an Al atom on the Ni sublattice and of a Ni on the Al sublattice, respectively, we obtain the difference of the formation energies to

$$E_{\mathrm{V}}^{(\mathrm{Al})} - E_{\mathrm{V}}^{(\mathrm{Ni})} = -4\epsilon_{\mathrm{AS}}^{(1)} + 6\epsilon_{\mathrm{AS}}^{(2)}\,. \tag{28}$$

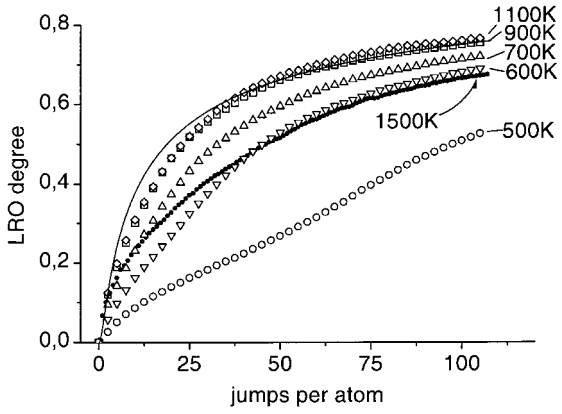

Fig. 14. LRO parameter *versus* number of atomic jumps according to the M.C. simulation. The solid line was calculated by equation (31) with $\gamma = 0.055$.

In accordance with the cited energy bias, we set $\epsilon_{\mathrm{AS}}^{(1)} = -0.2$ eV and $\epsilon_{\mathrm{AS}}^{(2)} = 0$. Using this parameter set, the M.C. model reproduces important features which are supposed to be fulfilled in the Ni_3Al structure. The vacancy concentration on the Ni sublattices exceeds that on the Al sublattice by several orders of magnitude as shown in Figure 13a. When the temperature of the system increases, the ratio between both concentrations follows an Arrhenius law as long as the degree of order remains unchanged. But approaching the critical temperature, the asymmetry between them decreases further due to the break down of the sublattice structure. The jump probability of an Al atom is much smaller than that of a Ni atom (see Fig. 13b). During the annealing, this bias increases with the evolving order. However, the absolute effect becomes less important at higher temperatures.

In order to characterize the state of order, the distribution function

$$c(x_{\mathrm{i}}) = \begin{cases} 1; & \text{if Al located at } x_{\mathrm{i}} \\ 0; & \text{else} \end{cases} \tag{29}$$

of the simulated configurations is Fourier transformed and the absolute value of the $\{011\}$ component of the spectrum is taken as a measure of ordering. To depress fluctuations due to the random anti-phase domain structure, the spectrum is averaged over a finite reciprocal volume close to the ideal frequency, similar to the way the intensity is averaged over a finite peak width when the experimental diffraction patterns are evaluated. In accordance with the experiment, the radius of the integration volume is chosen to be $r = 0.15\, a_0^{-1}$.

The ordering kinetics as predicted by the M.C. simulation are presented in Figure 14 at different temperatures. Since the LRO parameter is plotted *versus* the number of atomic jumps, the exponential temperature dependence of the average atomic mobility is already scaled out. Nevertheless, a significant temperature dependence is predicted by the simulation which clearly demonstrates that the efficiency of the atomic jumps α, is itself a function of temperature. This efficiency increases with the temperature

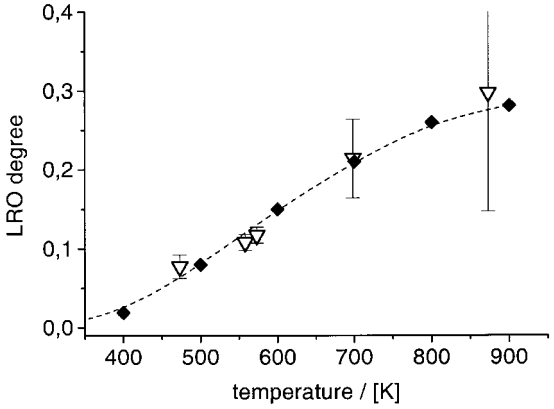

Fig. 15. Experimentally observed plateau values of the LRO parameter (triangles) in comparison with the result of the M.C. simulation after 9 jumps per atom (diamonds).

up to 900 K. Between 900 K and 1100 K the kinetics stay almost constant. Above 1200 K it slows down again for higher degrees of order, due to the decreasing driving force. It should be emphazised that the result of the microscopic simulation reveals no incubation period, opposite to the predictions for homogeneous ordering by Dienes or for the JMA kinetics. This behaviour may be understood by the extreme driving force due to the very stable order in Ni_3Al. The average kinetics at intermediate temperatures follows a root function which resembles domain ripening from the very beginning of the reaction. Assuming spherical domains with mean radius r and a disordered boundary layer of thickness δ we have [35]

$$s = \frac{(r-\delta)^3}{r^3}\,; \qquad r^2 - r_0^2 = \text{const.} \times j_\mathrm{a}\,. \tag{30}$$

Thus, setting $r_0 = \delta$, we obtain

$$s(j_\mathrm{a}) = \left(\frac{\sqrt{1+\gamma j_\mathrm{a}} - 1}{\sqrt{1+\gamma j_\mathrm{a}}}\right)^3. \tag{31}$$

Equation (31) describes the simulated kinetics at intermediate temperatures reasonably well as shown by the solid line in Figure 14 which was calculated with $\gamma = 1.2$. Compared to a first order kinetics, ordering drastically slows down at higher LRO degrees due to the domain ripening.

The kinetic behaviour revealed by the M.C. simulations represents the important key in understanding the temperature dependence of the observed LRO plateaus. In Figure 15 the experimental data for the order parameter after 3600 s annealing as determined in this work is compared with the order predicted after 9 jumps per atom by the M.C. simulation. Within the presented temperature range ($T < 900$ K) thermal vacancies do not influence the reaction. Beside the small discrepancy with the number of atomic jumps estimated by equation (13), the agreement between both data sets is striking which makes evident that the temperature dependence of the jump efficiency is essentially responsible for the observed ordering kinetics.

6 Discussion

From a microscopic point of view, the two phenomena – diffusion and ordering – are based on a unique mechanism, *i.e.* the exchange of atom-vacancy pairs. In order to study the correlation between these two phenomena, the investigation of so called 'order-order' transformations, where only small changes of the LRO parameter are involved, is advantageous as processes like nucleation and domain growth and artefacts due to non-equilibrium lattice defects do not complicate the reaction. Nevertheless, even in this case, controversial results were obtained regarding the activation energies of the Arrhenius-like temperature dependencies [3,4] which is presumably caused by different specimen treatments.

On the other hand, disordering by athermal processes such as vapor deposition, ball milling, and electron or ion irradiation allows much larger variations of the order degree and offers furthermore the possibility to vary the vacancy density independent of the temperature. In this way, specific information on the vacancy-atom exchange process may become obvious. The dominant influence of non-equilibrium vacancies after ball milling is demonstrated by small activation energies (1.6 eV to 1.8 eV) [8,9] which correspond quite well to the vacancy migration energy of Ni. Very recently, the annealing of non-equilibrium vacancies was explicitly taken into account to explain the recovery of SRO in such specimens [10]. Extrapolating the 'order-order' reaction kinetics determined by resistivity measurements between 700 K and 900 K [3,4] to the low reaction temperatures of this work, one obtains relaxation times of 10^{14} to 10^{24} s which clearly demonstrates that the reactions discussed here are only supported by non-equilibrium vacancies.

Based on the presented quantitative considerations, it is concluded from our experiments that the ordering evolves within a few tens of jumps per atom and that the ordering efficiency of the atomic replacements is temperature dependent, although the variation of the thermodynamic driving force is already separated. Concerning the relation between ordering and diffusion, this result is quite important as it allows preselection of possible microscopic jump models.

However, the argument requires the density of non-equilibrium vacancies to be deduced from the irradiation conditions under rather crude assumptions. As the spatial distribution of the irradiation defects is not known in detail, the formation of sessile clusters already during the irradiation was neglected. As long as such clusters keep stable, they simply increase the sink density and consequently reduce the number of atomic jumps. Only at high temperatures where these clusters dissolve, formerly sessile vacancies become mobile so that the number of atomic jumps may significantly increase. But any quantitative estimate at this stage would become very difficult. This effect probably explains the difference between the experimental data of this work and that presented in [26] (see Fig. 8). The latter data was obtained after irradiation by a ten-fold higher irradiation dose, which caused a much higher cluster density. Thus, it is not surprising

that at low temperatures the degree of order is smaller than determined in this work whereas above about 700 K the opposite is true. Nevertheless, the general tendency of a temperature dependent efficiency is observed in both experiments.

The reordering kinetics is well reproduced by the applied M.C. model, insofar as the absolute number of atomic jumps as well as the temperature dependence of the LRO plateaus are in agreement with the experimental data and the interaction parameters used are physically quite reasonable. Defining the jump mechanism by equation (15), it is assumed that the probability of a particular jump is controlled by the site energy of the initial as well as the possible final position. Thus, the vibrating atoms are expected to scan the stability of the vacant site before a stable site exchange is performed. By contrast, when a jump selection mechanism is applied, where the activation barrier is determined independently from the final site by the difference between a constant saddle point and the energy of the initial site, no agreement between the experiment and the simulation is achieved. In this case, the bias between the individual mobilities of Ni and Al is drastically overestimated and the temperature dependence of the kinetics becomes much too strong. At low temperatures (*e.g.* 500 K) the kinetics, when scaled *versus* the number of jumps per atom, is about two orders of magnitude too slow. As both jump models are well established for simulation work, this point should be further investigated. However, such an analysis is beyond the scope of this experimental study.

According to the simulated reactions, the temperature dependence of the jump efficiency is due to an asymmetry in the mobilities of the atomic species. Effective ordering only proceeds if both atom types have similar jump probabilities. At this point, details of the reordering mechanism become obvious, which are beyond the chemical reaction theory proposed by Dienes [33]. They are strictly related to the vacancy jump mechanism and the sublattice structure of the ordered lattice. Since the jump probabilities are essentially controlled by the $\epsilon_{\mathrm{AS}}^{(\mathrm{i})}$, the choice of these parameters is very important to obtain a reasonable temperature dependence in the modelling. Setting $\epsilon_{\mathrm{AS}}^{(1)} = \epsilon_{\mathrm{AS}}^{(2)} = 0$, up to 900 K all the kinetic curves in a plot like Figure 14 are identical.

The asymmetry parameters used in this work have been already justified above. Beside the cited first principle calculations, a higher vacancy formation energy on the Al sublattice may be justified by the heuristic argument that in order to generate a vacancy on the Al sublattice, 12 very strong bonds between unlike neighbours must be broken, whereas in the case of a vacancy on the Ni sublattice only four of these bonds are destroyed. Furthermore, from the cohesion energies of the pure elements, it is quite reasonable to assume $|\epsilon_{\mathrm{NiNi}}| > |\epsilon_{\mathrm{AlAl}}|$, so that an asymmetry between Ni and Al is also predicted in the disordered alloy. The M.C. method has the important advantage of describing both structures, the disordered alloy as well as the $L1_2$ ordered Ni_3Al within a unique frame, so that a continuous transition between both phases may easily be described.

7 Conclusion

The reordering kinetics of ion-irradiated Ni_3Al was determined by quantitative electron diffractometry. In addition, Monte-Carlo simulations were performed to allow interpretation of the experimental observations. The following points should be emphasized.

- An evaluation scheme for the measurement of LRO by quantitative electron diffraction is presented. By selecting a suitable specimen orientation, the sensitivity of the measurement may be adaptated to the required range of LRO degrees.
- After disordering the specimens by ion irradiation to 1 dpa, no reordering takes place at room temperature. However, significant reordering starts between 373 K and 473 K. Initially, the order reaction proceeds very fast reaching an apparent steady state of intermediate order.
- Up to 900 K, the observed reordering is dominated by the motion of non-equilibrium vacancies. As a consequence, the absolute number of vacancy jumps necessary to establish the detected order degree may be calibrated without relying on diffusion data.
- By selecting a suitable jump mechanism and reasonable interaction parameters, the reordering kinetics are simulated in accordance with the experimental results. The calculated development of the LRO degree corresponds to a domain growth mechanism from the very beginning of the reaction.
- In agreement with the experimental results, the simulations reveal that the ordering efficiency of vacancy jumps increases with temperature. This effect is based on the bias between the jump probabilities of Al and Ni which becomes more pronounced at low temperatures.

The authors thank F. Harbsmeier and M. Uhrmacher of the II. Physikalische Institut in Göttingen for their help in performing the ion irradiation and F. Haider, Augsburg University and C. Abromeit, HMI in Berlin, for many valuable discussions. The financial support by the DFG is gratefully acknowledged.

References

1. R.W. Cahn, P.A. Siemers, J.E. Geiger, P. Bardhan, Acta Metall. **35**, 2753 (1987).
2. H. Numakura, T. Ikeda, M. Koiwa, A. Almazouzi, Phil. Mag. A **77**, 887 (1998).
3. C. Dimitrov, X. Zhang, O. Dimitrov, Acta Mater. **44**, 1691 (1996).
4. R. Kozubski, Prog. Mat. Sci. **41**, 1 (1997).
5. A.R. Yavari, B. Bochu, Phil. Mag. A **59**, 697 (1989).
6. S.R. Harris, D.H. Pearson, C.M. Garland, B. Fultz, J. Mater. Res. **6**, 2019 (1991).
7. A. Yavari, Acta Met. Mater. **41**, 1391 (1993).

8. e.a. M.D. Baro, Acta Met. Mat. **41**, 1065 (1993).
9. e.a. F. Cardellini, J. Mat. Res. **8**, 2504 (1993).
10. P. Scherrer, S.R.C. Dimitropoulos, F. Borsa, Phys. Rev. A **57**, 10462 (1998).
11. G. Carpenter, E. Schulson, Scripta Metall. **15**, 549 (1981).
12. H. Liu, T. Mitchell, Acta Metall. **31**, 863 (1983).
13. O. Dimitrov, C. Dimitrov, Intermetallics **2**, 249 (1994).
14. C. Abromeit, S. Mueller, N. Wanderka, Scripta Metall. **32**, 1519 (1995).
15. S. Mueller, M.L. Jenkins, C. Abromeit, H. Wollenberger, Phil. Mag. **75**, 1625 (1997).
16. J.C. Ewert, G. Schmitz, F. Harbsmeier, M. Uhrmacher, F. Haider, Appl. Phys. Lett. **73**, 3363 (1998).
17. M. Uhrmacher, K. Pampus, F.J. Bergmeister, D. Purschke, K. Lieb, J. Nucl. Mat. B **9**, 234 (1985).
18. J. Ziegler, J. Biersack, V. Littmark, *The Stopping and Range of Ions in Solids* (Pergamon, New York, 1985).
19. G. Carpenter, E.M. Schulson, J. Nucl. Mater. **73**, 180 (1978).
20. N. Njah, D. Gilbon, O. Dimitrov, J. Nucl. Mater. **199**, 237 (1993).
21. K. Urban, Physica Status Solidi (a) **87**, 459 (1985).
22. P.A. Doyle, P.S. Turner, Acta Crystallogr. Sect. A **24**, 390 (1968).
23. P.A. Stadelmann, Ultramicroscopy **21**, 131 (1987).
24. J.M. Cowley, *Diffraction physics* (New York, 1975).
25. J. Gjonnes, J. Tafto, Ultramicrosopy **52**, 445 (1994).
26. S. Müller, Ph.D. thesis, TU Berlin, 1997.
27. C. Fu, G. Painter, Acta mater. **45**, 481 (1997).
28. H.J. Wollenberger, in *Physical Metallurgy*, edited by R.W. Cahn, P. Haasen (North-Holland Physics Publishing, Amsterdam, 1983).
29. R. Sizmann, J. Nucl. Mater. **69**, 386 (1978).
30. V. Naundorf, M.-P. Macht, H. Wollenberger, J. Nucl. Mater. **186**, 227 (1992).
31. G. Dienes, G. Vineyard, *Radiation effects in solids* (Interscience Publishers, New York, 1957).
32. C. Abromeit, V. Naundorf, Intermetallics **4**, 441 (1996).
33. G. Dienes, Acta Metall. **3**, 549 (1955).
34. F. Haider, habil. thesis, Univ. Göttingen, 1994.
35. G. Sauthoff, Acta Metall. **21**, 273 (1973).
36. H. Mehrer, *Landolt-Börnstein* (Springer, Berlin, 1990), Vol. 26.